Article

Deterministic photon source of genuine three-qubit entanglement

Yijian Meng[1], Ming Lai Chan [1], Rasmus B. Nielsen[1], Martin H. Appel [1,3], Zhe Liu[1], Ying Wang[1], Nikolai Bart[2], Andreas D. Wieck [2], Arne Ludwig[2], Leonardo Midolo [1], Alexey Tiranov [1,4], Anders S. Sørensen [1] & Peter Lodahl [1] ✉

Deterministic photon sources allow long-term advancements in quantum optics. A single quantum emitter embedded in a photonic resonator or waveguide may be triggered to emit one photon at a time into a desired optical mode. By coherently controlling a single spin in the emitter, multi-photon entanglement can be realized. We demonstrate a deterministic source of three-qubit entanglement based on a single electron spin trapped in a quantum dot embedded in a planar nanophotonic waveguide. We implement nuclear spin narrowing to increase the spin dephasing time to $T_2^* \simeq 33$ ns, which enables high-fidelity coherent optical spin rotations, and realize a spin-echo pulse sequence for sequential generation of spin-photon and spin-photon-photon entanglement. The emitted photons are highly indistinguishable, which is a key requirement for scalability and enables subsequent photon fusions to realize larger entangled states. This work presents a scalable deterministic source of multi-photon entanglement with a clear pathway for further improvements, offering promising applications in photonic quantum computing or quantum networks.

Foundational quantum photonics devices are rapidly developing towards real-world applications for advanced quantum communication and quantum computation[1–3]. The general scaling-up strategy is to utilize small-size entangled states as seeds that can subsequently be fused by probabilistic linear optics gates to realize a universal resource for quantum-information processing[4–10]. Traditionally these entangled seed states have been generated with probabilistic sources; however, a massive overhead of multiplexing is required to make this approach scalable[11].

An alternative and resource-efficient strategy has been proposed for the deterministic generation of multi-photon entangled seed states using a single quantum emitter[12,13]. Recent experimental work on multi-photon entanglement generation has made significant progress both using single atoms[14] and quantum dots[15–18]; in the former case an

impressive 14-photon high-fidelity deterministic entangled source was realized. Yet solid-state alternatives remain attractive due to their high speed and ease of operation, and potential scalability to multiple emitters[19]. These features are essential when constructing realistic architectures for scaled-up quantum-information processing based on deterministic entanglement sources[7].

Previous work on solid-state emitters has been limited to either two-qubit entanglement[15,20], or relied on theoretical assumptions to infer multi-particle entanglement[16–18]. Ref. 16 measured two-qubit correlations and used them to determine the full process map of a single entanglement cycle. Repeated application of the process map was then used to reconstruct an n-photon cluster state and infer an entanglement length of ten photons. The validity of this procedure requires that imperfections between different cycles are uncorrelated,

[1]Center for Hybrid Quantum Networks (Hy-Q), The Niels Bohr Institute, University of Copenhagen, Copenhagen Ø, Denmark. [2]Lehrstuhl für Angewandte Festörperphysik, Ruhr-Universität Bochum, Universitätsstraße 150, Bochum, Germany. [3]Present address: Cavendish Laboratory, University of Cambridge, JJ Thomson Avenue, Cambridge, United Kingdom. [4]Present address: Chimie ParisTech, Université PSL, CNRS, Institut de Recherche de Chimie Paris, Paris, France. ✉e-mail: lodahl@nbi.ku.dk
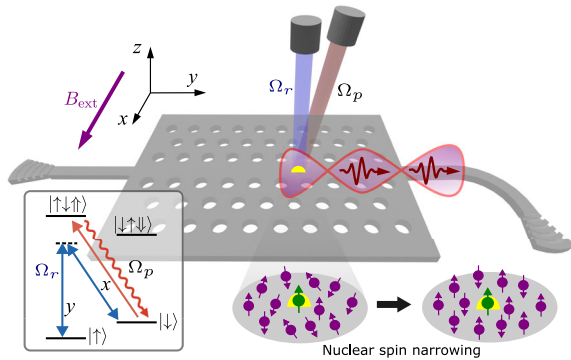
Fig. 1 | Deterministic GHZ state generation from a QD embedded in a PCW. A three-qubit GHZ state is realized by entangling the QD (yellow dot) electron spin and two QD-emitted single photons (red wavepackets). We collect the single photons through the PCW and couple them to free space via a grating outcoupler. The QD electron spin (dark green arrow) is subjected to the Overhauser field induced by nearby nuclear spins (purple arrows). To improve T_2^* of the electron spin, we reduce fluctuations of the Overhauser field by employing nuclear spin narrowing. The QD is operated in the Voigt geometry with an in-plane magnetic field of 4 T along the x-axis. The energy level scheme of the QD is presented in the inset. The Raman laser Ω_r (blue) is used for coherent spin manipulation of two Zeeman ground states $|\uparrow\rangle$ and $|\downarrow\rangle$. To generate single photons, a picosecond pulsed laser Ω_p (red) drives photon emissions on the diagonal cycling transition $|\downarrow\rangle \rightarrow |\uparrow\downarrow\Uparrow\rangle$. The same transition is used for the spin readout. Spin initialization is realized through optical pumping on the non-cycling transition $|\downarrow\rangle \rightarrow |\downarrow\uparrow\Downarrow\rangle$.

i.e., a purely Markovian noise process. Ref. 17 also measured two-qubit correlations and inferred a lower bound on the three-qubit entanglement fidelity based on two hypotheses: 1) the spin initializes in a perfect mixed state at the beginning of the entanglement sequence, and 2) two successive photons emission having the same polarization after spin initialization. While the assumptions of these studies can be reasonable and are, to some extent, justified by additional measurements, they lack a direct measurement of the density matrix of the generated three-qubit state. Moreover, a related demonstration was conducted for a source with limited indistinguishability in ref. 18, but it only demonstrated three-partite entanglement by 1.5 standard deviations and did not implement active spin control as required for scalability.

In this work, we directly verify genuine three-qubit entanglement with a solid-state quantum-dot (QD) source. High-fidelity realization of such states has been proposed as the fundamental building block of quantum computing architectures[5]. The generated three-qubit Greenberger-Horne-Zeilinger (GHZ) state consists of one electron spin and two photons. Without any theoretical assumptions or background subtraction, we measure a quantum state fidelity of 56(2)% and single photon indistinguishability exceeding 90%. Further data analysis demonstrates genuine three-qubit entanglement through violation of a biseparablity criteria by 10 standard deviations.

Results

We realize a recently proposed time-bin multi-photon entanglement protocol[21,22]. The protocol proceeds by entangling the QD spin with the emission time of deterministically generated single photons[21,22]. Previous works require the natural spin precession at a low magnetic field (few mT)[16–18]. For such an approach, scaling up to higher numbers of entangled qubits requires increasing the number of spin precessions within the short spin dephasing time (≈ 2 ns for electron spin), but reducing the precession period is at odds with producing indistinguishable photons from two ground states separated by the precession frequency and this constrains the fidelity. In contrast, we operate in the regime of a strong Voigt magnetic field which enables active spin control and clearly distinguishable optical transitions. The former allows for preserving the spin coherence in a noisy solid-state

environment via spin-echo sequences and nuclear spin narrowing. The latter is essential for high photon indistinguishability, enabling fusion operations between different seed states.

In our previous work on deterministic entanglement generation, the entanglement fidelity was primarily limited by the quality of optical spin rotations[15]. There a hole spin was applied since the inhomogeneous spin dephasing time $T_2^* \approx 20$ ns was several times longer than the duration of a π pulse on the spin ($T_p = 7$ ns), which is the key requirement for the protocol. However, the laser rotation pulses were found to induce incoherent (T_1) spin-flip errors of the hole spin, which limited the π-rotation fidelity to $F_\pi \approx 88\%$. This error alone sets an upper bound to the two-qubit entanglement fidelity to 77%.

To resolve this bottleneck, we employ the electron spin since the laser-induced spin-flip rate (κ) has been shown to be an order of magnitude lower[23]. Conversely, the electron dephasing time is inherently short $T_2^* \approx 2$ ns[24] and therefore must be prolonged in order to enable high-fidelity spin rotations. To this end, we implement nuclear spin narrowing by optical coupling[25], see Fig. 1, whereby the spin nuclear noise is significantly reduced and T_2^* prolonged. The nuclear spin ensemble couples to the electron spin via the Overhauser field, where the shift of the electron spin resonance (ESR) is proportional to the net polarization of the nuclei I_z. In the presence of material strain, optical rotations on the electron spin mediate the nuclear spin-flip transition. By driving and resetting the electron spin with two optical pulses, I_z converges toward a stable point such that its fluctuations are suppressed.

The single-photon emitter is a self-assembled InAs QD embedded in a GaAs photonic-crystal waveguide (PCW) inside a closed cycle cryostat held at 4 K. The QD is grown in a tunable p-i-n diode heterostructure where a bias voltage charges the QD with an electron as the spin qubit. An external magnetic field of $\mathbf{B}_x = 4$ T is applied (Voigt geometry), which Zeeman splits the electron spin ground state into $|\uparrow\rangle$ and $|\downarrow\rangle$ by $\Delta_g = 22$ GHz and excited state into $|\uparrow\downarrow\Uparrow\rangle$ and $|\downarrow\uparrow\Downarrow\rangle$ by $\Delta_e = 12$ GHz, resulting in four optical transitions.

The PCW offers distinct advantages in the time-bin entanglement protocol. First, the close-to-unity on-chip coupling efficiency ($\beta > 98\%$ experimentally demonstrated[26]) allows scalable operation towards large photon states, which can be further evanescently coupled to a reconfigurable quantum photonic circuit with a very low loss[27,28]. Second, the PCW generally Purcell enhances one linear dipole and suppresses the orthogonal dipole, leading to an inherently large optical cyclicity in the Λ-level scheme, where a spin-preserving optical transition and spin rotating Raman transitions can both be implemented[29]. We find that the decay rate of the inner (outer) optical transition γ_X (γ_Y) to be enhanced (suppressed) and measured a cyclicity of $C = \gamma_X/\gamma_Y = 36(3)$, which is the highest recorded value for QDs in the Voigt geometry and an essential figure-of-merit for the entanglement protocol[30].

The GHZ generation protocol utilizes spin-dependent emission of a single photon, and when combined with coherent spin rotations, it allows entanglement generation between the spin state and the time bin of emitted photons[15], see Fig. 2. First, a $\pi/2$-rotation pulse prepares the spin in a superposition state $(|\uparrow\rangle - |\downarrow\rangle)/\sqrt{2}$. A picosecond laser pulse then drives the cycling transition $|\downarrow\rangle \rightarrow |\uparrow\downarrow\Uparrow\rangle$, see inset of Fig. 1, resulting in the single-photon emission in the early time bin. A spin π-rotation pulse subsequently swaps the $|\uparrow\rangle$ and $|\downarrow\rangle$ population and a second picosecond laser pulse potentially creates a photon in a later time bin. The last π-pulse swaps spin population again, resulting in the Bell state $(|e\downarrow\rangle - |l\uparrow\rangle)/\sqrt{2}$. By iterating this pulse sequence $n-1$ times (apart from the first $\pi/2$-pulse), a GHZ state of $n-1$ photonic qubits and one spin qubit $|\psi_{GHZ}\rangle = (|0\rangle^{\otimes n} - |1\rangle^{\otimes n})/\sqrt{2}$ is generated, where we translate $|\downarrow\rangle(|\uparrow\rangle)$ and early(late) emitted photon into the logical qubit $|0\rangle(|1\rangle)$.

Characterization of spin control after nuclear spin narrowing

Prior to running the entanglement protocol, we first characterize the quality of spin control by performing Ramsey spectroscopy and
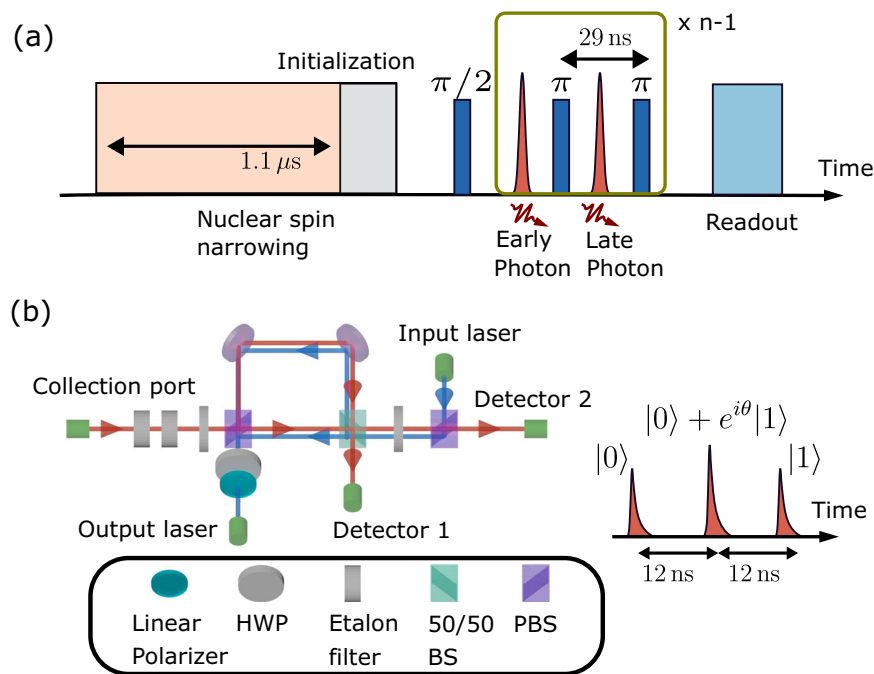
Fig. 2 | Schematic diagram of time-bin GHZ state generation. a The experimental sequence consists of nuclear spin narrowing and spin initialization, which is then followed by the GHZ protocol with a series of $\pi/2$, π-pulses (blue) and single photon generations (red). The last part of the sequence (enclosed in the box) is repeated $n-1$ times to generate an n qubit GHZ state. The duration of the full sequence is 1.8 μs. Nuclear spin narrowing consists of two overlapped 1.1 μs Raman pulse and a 1.2 μs pump pulse. The longer pump pulse optically drives the $|\downarrow\rangle \rightarrow |\downarrow\uparrow\Uparrow\rangle$ transition and initializes the spin state to $|\uparrow\rangle$ before the GHZ state generation. **b** Time bin interferometer (TBI) setup: A picosecond pulsed laser (blue) propagates through the long and short arm of TBI to excite a QD emitting a single photon in the early and late time bin, respectively. The single photon is collected through the same TBI but in the opposite direction. Each photonic qubit has three peaks in the output that are separated by 12 ns, which is determined by the path-length difference between the long and short arms of the TBI.

observing Rabi oscillations after nuclear spin narrowing. In the former, we initialize the electron spin in $|\uparrow\rangle$ by optically pumping $|\downarrow\rangle \rightarrow |\downarrow\uparrow\Uparrow\rangle$ and vary the time delay T_d between two $\pi/2$-rotation pulses. The pulses are -200 MHz detuned from the spin transitions to reveal oscillations of the Ramsey decay with T_d, see Fig. 3a. We model the Ramsey data assuming a Gaussian decay and find $T_2^* = 33(3)$ ns, which is one order of magnitude longer than the spin π-rotation pulse of $T_p = 4$ ns used in the GHZ generation sequence, thus enabling high rotation fidelity. In Fig. 3b, we drive the spin with a rotation pulse of varying duration T_p to observe Rabi oscillations between $|\uparrow\rangle$ and $|\downarrow\rangle$. We extract a spin Rabi frequency of $\Omega_r = 2\pi \cdot 123.6$ MHz and a quality factor of Q = 34(2), i.e., Q quantifies the number of π-pulses before the oscillation visibility falls to $1/e$. We estimate the π-rotation fidelity via $F_\pi = \frac{1}{2}(1 + e^{-1/Q}) \approx 98.6\%$[23]. For comparison, the π-rotation fidelity error due to finite T_2^* is $2/(\Omega_r T_2^*)^2 = 0.3\%$[31], and we attribute the remaining fidelity error to laser-induced spin-flip processes[15,23]: $\frac{1}{2}(1 - e^{-\pi\tilde{\kappa}})$. The extracted normalized spin-flip rate is $\tilde{\kappa} = \kappa/\Omega_r \approx 3 \times 10^{-3}$, which is an order of magnitude lower compared to the case of a hole spin[15].

To shield the electron spin qubit against nuclear spin noise, the GHZ generation protocol exploits a built-in spin-echo sequence. We now discuss the spin-echo sequence and benchmarks of the spin coherence. The spin echo consists of three equally spaced $\pi/2$, π, and $\pi/2$-rotation pulses. We measure the spin echo visibility as a function of the spacing between the pulses. The fringe visibility at each spacing is extracted by altering the phase shift of the last $\pi/2$-pulse between 0 and π relative to the previous pulses. We observe a rapid decay of the visibility and a subsequent revival at $T_s \approx 29$ ns, see Fig. 3c. The revival peak is located approximately at the inverse of the Larmor frequency of Indium nuclear spins at 4 T[32]. The optimal pulse delay corresponding to the peak is then adopted in the entanglement protocol. The maximum spin-echo visibility is 76%, which constitutes a 20% improvement over previous work[15]. This is an essential figure-of-merit

contributing to fidelity of the multi-photon entanglement, as discussed later.

We model the data of Fig. 3(c) using the nuclear noise spectral density in InAs QDs as presented by Stockill et al.[32]. Very good agreement is reached where the observed coherence revival is reproduced. In the model, we consider the linearly coupled Overhauser field components along the quantization axis of the electron and only use the overall amplitude as a free parameter. We fit the data at $T_s \geq 3$ ns, where the observed discrepancy between data and model at shorter time delays is attributed to interference between the driving pulses. Details of the theoretical model are presented in Supplementary Section VIII.B. The quantitative understanding of the spin-echo visibility is essential for pinpointing how to improve the spin-photon entanglement fidelity in future experiments.

We also perform an extended experiment with two additional π-pulses at the same spacing, i.e., a pulse sequence of $\pi/2 \cdot \pi \cdot \pi \cdot \pi \cdot \pi/2$, and find a maximum echo visibility of 65%. Compared to the 3-qubit GHZ generation protocol, this measurement is free from excitation errors associated with single-photon generation, the measured visibility therefore poses an upper bound on the three-qubit correlations along the equatorial plane of the Bloch sphere.

GHZ state generation and fidelity analysis

The GHZ state is generated and analyzed with the self-stabilized time-bin interferometer in Fig. 2b[15]. For the photonic qubit, the output consists of three peaks. The first (last) peak corresponds to early (late) emitted photons going through the short (long) arm and constitutes a measurement in the $|1\rangle$ ($|0\rangle$) basis. The middle peak corresponds to the early photon going the long arm and the late photon going through the short arm, corresponding to the $|0\rangle + e^{i\theta}|1\rangle$ basis, where θ is readily controlled via a stack of waveplates and a polarizer[15]. By changing θ, the photonic qubit is measured on the equatorial basis of
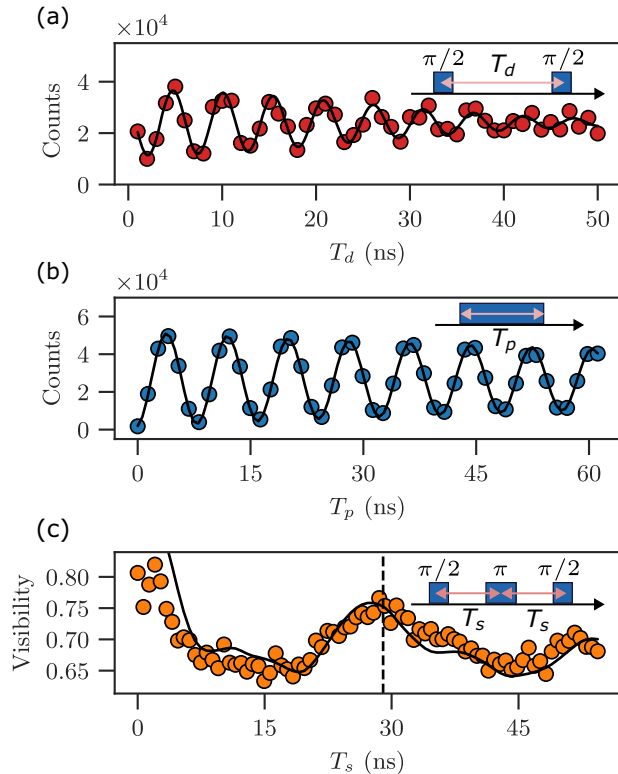
Fig. 3 | Electron spin spectroscopy. a and **b** display Ramsey interference and Rabi oscillation data, respectively. We use the former data to extract a spin coherence time of $T_2^* = 33(3)$ ns, where we model the data by assuming inhomogeneous broadening with a Gaussian distribution. From the Rabi oscillation data, we extract a Q-factor of 34(2). **c** shows the Hahn-echo visibility as a function of the spacing between the center of $\pi/2$-pulses and the middle π-pulse. The solid black line is a model of the data by including the nuclear noise spectrum. The dashed-vertical line indicates the echo-pulse spacing used in the GHZ entanglement generation experiment.

the Bloch sphere. Spin readout is performed by optically driving the cycling transition $|\downarrow\rangle \rightarrow |\uparrow\downarrow\Uparrow\rangle$ with a 200 ns pulse. Since only photons are emitted when the spin state is $|\downarrow\rangle$, an additional π-pulse is applied before the readout to measure $|\uparrow\rangle$. Similarly, to measure the spin qubit on the equatorial plane, a $\pi/2$ pulse is performed instead.

The entanglement fidelity is decomposed as $\mathcal{F}_{GHZ} = \text{Tr}\{\rho_{exp}|\psi_{GHZ}\rangle\langle\psi_{GHZ}|\} = \text{Tr}\{\rho_{exp}(\hat{\mathcal{P}}_z + \hat{\chi})/2\}$[33], where $|\psi_{GHZ}\rangle$ is the ideal GHZ state and ρ_{exp} is the experimentally measured density matrix. $\hat{\mathcal{P}}_z = |0\rangle\langle0|^{\otimes n} + |1\rangle\langle1|^{\otimes n}$ projects all qubits on the z-basis and $\hat{\chi} = |0\rangle\langle1|^{\otimes n} + |1\rangle\langle0|^{\otimes n} = \frac{1}{n}\sum_k(-1)^k\hat{\mathcal{M}}_k$ is composed of $\hat{\mathcal{M}}_k$ operators that are equally spread along the x-y plane of the Bloch sphere, see Fig. 4c. The measurement of each operator proceeds from three-photon coincidences between two photonic qubits and a photon from the spin readout in their respective bases. The normalized three-fold coincidences in each basis are shown in Fig. 4a–b. From here the state fidelity is found to be $\mathcal{F}_{GHZ} = 56(2)\%$, where $\langle\hat{\mathcal{P}}_z\rangle$ and $\langle\hat{\mathcal{M}}_{1,2,3}\rangle$ are 76(2)% and −40(5)%, 35(4)%, −33(4)%, respectively. In the present experiment, the 3-qubit generation rate is estimated to be $R_{GHZ} = \eta_p^2 R_{exp} \simeq 70$ kHz, with the experimental repetition rate of $R_{exp} = 560$ kHz. The photon efficiency η_p includes less-than-π optical excitation (80% due to 0.7π excitation pulse), emission into the zero-phonon line (95%)[34], the two-sided waveguide geometry (50%), and waveguide coupling efficiency ($\beta \approx 90\%$)[35]. Additional off-chip loss of the entanglement characterization setup constitutes ≈ 14 dB (see Sec. XI of Supplementary Material). Immediate optimization opportunities include operating on a single-sided waveguide[28] and increasing the operation speed to $R_{exp} = 1$ MHz with a reduced nuclear spin narrowing duty cycle,

whereby $R_{GHZ} = 0.5$ MHz is immediately reachable. For subsequent applications of the entanglement source, high-efficiency outcoupling strategies from the chip to the optical fiber can be readily implemented[28].

As a complementary entanglement characterization, we also measure biseparability of the generated state, whereby violation of the following inequality implies genuine three-qubit entanglement: $|\chi| \leq \sqrt{\rho_{001}\rho_{110}} + \sqrt{\rho_{110}\rho_{001}} + \sqrt{\rho_{101}\rho_{010}}$[36]. For our experiment, the left and right hand side of the inequality equates to $\langle\hat{\chi}\rangle = 35.8(2.5)\%$ and $9.6(1.1)\%$, respectively. The inequality is violated by 10 standard deviations, providing a clear demonstration of genuine 3-particle entanglement.

Fidelity error contribution and future outlook

To unravel experimental imperfections, we have performed detailed Monte-Carlo simulations including all relevant physical errors, see Supplementary Sections VIII and IX for full details. For the 3-qubit GHZ state, we predict $\mathcal{F}_{GHZ}^{sim} = 57.1(8)\%$, which is in very good agreement with the recorded experimental value. Table 1 lists the three main sources of fidelity error. The largest contribution originates from optical excitation of the unwanted cycling transition $|\uparrow\rangle \rightarrow |\downarrow\uparrow\Downarrow\rangle$, since the two cycling transitions (the diagonal transitions in Fig. 1) are only frequency split by $\Delta = 10$ GHz, which is similar to the excitation laser bandwidth (12.5 GHz). To minimize off-resonant excitation, we excite via an optical 0.7π pulse at a frequency 2 GHz red-detuned from the targeted cycling transition $|\downarrow\rangle \rightarrow |\uparrow\downarrow\Uparrow\rangle$. For future experiments, this excitation error could be almost entirely mitigated by orienting the waveguide in the orthogonal direction so that the vertical transitions become cycling.

The second largest error contribution is the high-frequency nuclear spin noise that was responsible for the reduced spin-echo visibility in Fig. 3c, which then manifests as fidelity error in the entanglement protocol. The noise spectrum is strain dispersion dependent and therefore will constitute a fundamental limit for strain-induced grown QDs (Stranski-Krastanov method) such as InAs QDs in GaAs, but droplet-epitaxy GaAs QDs have proven to be significantly less noisy[37]. Finally, the third main contribution stems from rotation errors due to laser-induced spin flips. A lower rotation error has been observed in a GaAs QD device[37] and the lack of a blocking barrier in these devices suggests a similar design to mitigate laser-induced spin flips in InAs QDs.

In future experiments, we can readily eliminate the first and the most dominant error source by rotating the PCW by 90°, leading to a Purcell-enhanced y-dipole, see Fig. 1 inset. In this configuration, the two transitions with the highest energy difference are cycling transitions with a frequency splitting of ≈ 30 GHz. Consequently, this would allow generating 3 and 4-qubit GHZ states with fidelity of 67% and 58%, respectively (See Sec. VIII of Supplementary Material). Improving beyond this would require reducing the two latter errors. To this end, GaAs QDs have proven to be a highly promising platform. From the numerical simulations, we predict 8.8(1)% fidelity error per photon for GaAs QDs, meaning that GHZ strings of 8 qubits should be attainable, where we have used the QD parameters reported in ref. 37. Figure 5 summarizes the experimental and simulated findings of the GHZ state fidelity for the various experimental situations.

Single-photon purity and indistinguishability measurements

Finally, to characterize the quality of emitted photons, we perform Hanbury-Brown-Twiss (HBT) and Hong-Ou-Mandel (HOM) interferometry to measure single-photon purity and indistinguishability, respectively[29]. Here we use a different experimental sequence where we initialize the spin in $|\downarrow\rangle$ with a π-rotation pulse, and excite the QD twice with the pulsed laser. The pair of emitted photons propagate through TBI and arrive at two detectors in the early, middle and late time bins, which align to the three peaks in Fig. 2(b). For HBT, we look
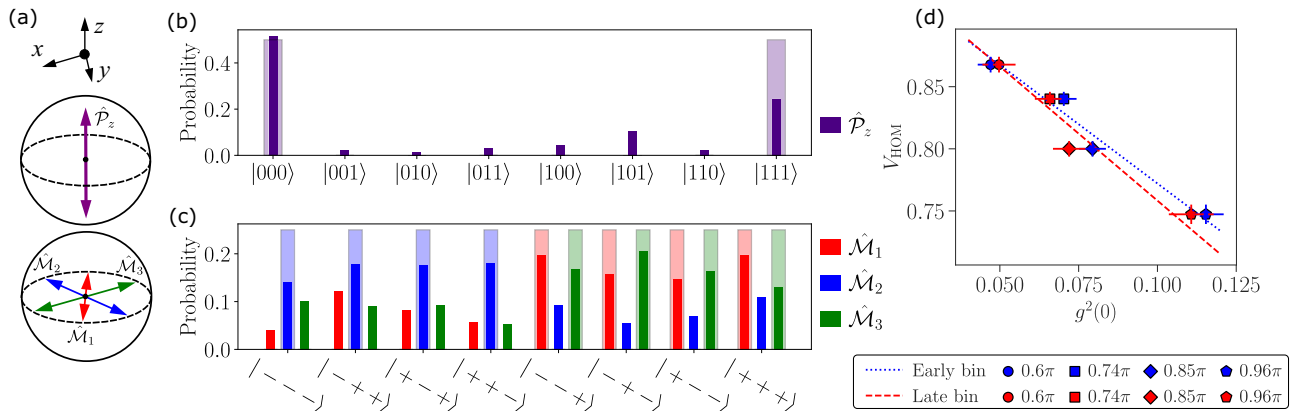
Fig. 4 | Fidelity measurement of 3-qubit GHZ state and single-photon characterization. a Illustration of the measurement basis on the Bloch sphere. **b**, **c** Histogram of fidelity measurement in the z-basis and x, y-basis, respectively. In **c**, $|+\rangle$ and $|-\rangle$ are eigenstates of the operator $\hat{\mathcal{M}}_i$. The acquisition time for each operator is ~2 h. The shaded bars 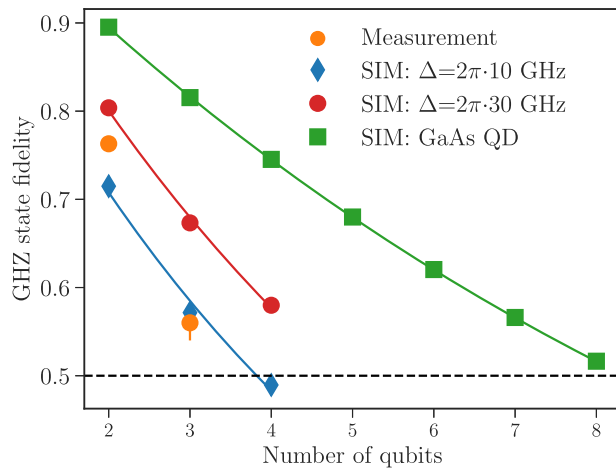in (**a**–**c**) indicate the ideal cases. **d** Measurement of HOM visibility and single-photon purity at different excitation powers (normalized to the π-pulse power). Single-photon indistinguishability V_s is extracted from the y-intercept of the linear extrapolation. $g^{(2)}(0)$ is measured in the first and third time bins whereas V_{HOM} is measured in the second time bin, see main text. The error bars represent one standard deviation.

Table 1 | Fidelity error contribution of the three primary simulated errors

Primary error sources	Fidelity error
Off-resonant excitation	11.4 %
Nuclear spin noise	6.0 %
Spin-flip error during rotation	3.2 %

The value of the fidelity error contribution is calculated as the difference between the fidelity with and without the error source.

Fig. 5 | Summary of experimental results and outlook for future experiments. Results of three Monte Carlo simulations (SIM): with the current splitting between cycling transitions $\Delta = 2\pi \cdot 10$ GHz, with the expected modification of a larger $\Delta = 2\pi \cdot 30$ GHz corresponding to properly oriented waveguides relative to the dipole axes, and with GaAs QD where the effect of nuclear spin noise is negligible and we assume $\Delta = 2\pi \cdot 30$ GHz and a π spin rotation fidelity improved by a factor of 2[37]. For all parameters, we run Monte Carlo simulation (10^4 realizations) from 2 to 4 qubits, while the fidelity of higher qubit numbers is extrapolated with an exponential fit. For GaAs QD, N_{max} is the predicted maximum attainable number of entangled qubits from the fit, given that $\mathcal{F}_{GHZ}$ is one standard deviation above 50%. The minor deviation between measurement and simulation is likely due to an overestimation of the nuclear spin noise and an underestimation of other experimental errors, e.g., an imperfect excitation laser polarization.

at two-detector coincidences in the early or late time bin. We extract $g^{(2)}(0)$ from the ratio between coincidence counts occurring in the same experimental cycle and two consecutive cycles. For HOM, we extract the HOM visibility V_{HOM} by recording two-detector coincidence counts in the middle bin, normalized to coincidences between the middle bin in one detector and early or late time bin in the other detector. We measure both V_{HOM} and $g^{(2)}(0)$ for a range of excitation powers, see Fig. 4(d).

Setups	N_{max}	Fidelity error per photon
Measurement	3 ($\mathcal{F}_{GHZ} = 56(2)\%$)	27(3)%
SIM: $\Delta = 10$ GHz	3 ($\mathcal{F}_{GHZ} = 57.1(8)\%$)	17(2)%
SIM: $\Delta = 30$ GHz	4 ($\mathcal{F}_{GHZ} = 58.0(8)\%$)	15(1)%
SIM: GaAs QD	8 ($\mathcal{F}_{GHZ} = 51.6(4)\%$)	8.8(1)%

The intrinsic single-photon indistinguishability V_s would be measured in HOM interferometry if the multi-photon contribution and laser leakage were negligible, i.e., $g^{(2)}(0) = 0$. We observe a close to linear relationship between V_s and $g^{(2)}(0)$. Using linear regression, i.e., $V_{HOM} = V_s - F \cdot g^{(2)}(0)$[38], we obtain $F = 2.0(3)$ and $V_s = 97(2)\%$ after averaging over the data acquired at the first and last time bins. While $F = 2$ has been widely used in the literature[39,40], the relationship between $g^{(2)}(0)$ and V_s can be more complicated where F varies between 1 and 3, depending on the origin of the multi-photon contribution[41]. $F \approx 2$ indicates that the recorded V_{HOM} is primarily limited by distinguishable multi-photon component, which could potentially be removed at the cost of lower brightness, e.g., by time gating. To reduce laser leakage, we perform additional frequency filtering using a pair of etalon filters (with a full width at half maximum of 3 GHz) before the TBI. We note the indistinguishability has a lower bound of 92(1)% when $F = 1$. The high degree of indistinguishable photons means that the demonstrated entanglement source is readily applicable for realizing photon fusion, which is the essential operation enabling photonic quantum computing[6].

Discussion

We have presented a direct demonstration of the on-demand generation of a genuine three-qubit entangled state using a QD spin-

photon interface. This realizes a foundational building block for scalable photonic quantum-information processing towards photonic quantum computers[6] or one-way quantum repeaters[42]. The full account of entanglement infidelities is laid out, which is essential for further improvements of the approach in future experiments.

The InAs QD platform is predicted to be scalable to strings of 4 entangled qubits (Fig. 5), which suffices for implementing small-scale measurement-based quantum algorithms. Importantly, the high degree of indistinguishability means that such a source can be used to fuse much larger entangled states by de-multiplexing the photons[43] and subsequently interfering them in, e.g., an integrated photonic circuit. Interestingly, the current limitation to fidelity can be overcome with a straightforward correction of the device orientation, thanks to a larger splitting between two cycling transitions Δ. We expect the next iteration of the experiment to go to 3 photons and 1 spin, limited by the rotation fidelity error and nuclear spin noise. Longer strings of entangled photons may be realized with strain-free GaAs droplet-epitaxy QDs, where the π-spin rotation error is halved and the high-frequency nuclear noise with a narrower spectrum can be effectively filtered[37]. Such deterministic entanglement sources relying on spin-photon interfaces may offer fundamentally new opportunities for resource-efficient photonic quantum computing architectures[8,9].

Data availability
Data can be found in the following repository: https://erda.ku.dk/archives/89bd3313cade9bf037f936f75420d09e/published-archive.html.

References

1. Raussendorf, R., Browne, D. E. & Briegel, H. J. Measurement-based quantum computation on cluster states. *Phys. Rev. A* **68**, 022312 (2003).
2. Walther, P. et al. Experimental one-way quantum computing. *Nature* **434**, 169–176 (2005).
3. Zhang, R. et al. Loss-tolerant all-photonic quantum repeater with generalized Shor code. *Optica* **9**, 152 (2022).
4. Rudolph, T. Why I am optimistic about the silicon-photonic route to quantum computing. *APL Photonics* **2**, 030901 (2017).
5. Gimeno-Segovia, M., Shadbolt, P., Browne, D. E. & Rudolph, T. From three-photon greenberger-horne-zeilinger states to ballistic universal quantum computation. *Phys. Rev. Lett.* **115**, 020502 (2015).
6. Bartolucci, S. et al. Fusion-based quantum computation. *Nat. Commun.* **14**, 912 (2023).
7. Uppu, R., Midolo, L., Zhou, X., Carolan, J. & Lodahl, P. Quantum-dot-based deterministic photon–emitter interfaces for scalable photonic quantum technology. *Nat. Nanotechnol.* **16**, 1308–1317 (2021).
8. Löbl, M. C., Paesani, S. & Sørensen, A. S. Loss-tolerant architecture for quantum computing with quantum emitters. *Quantum* **8**, 1302 (2024)
9. Paesani, S. & Brown, B. J. High-threshold quantum computing by fusing one-dimensional cluster states. *Phys. Rev. Lett.* **131**, 120603 (2023).
10. Istrati, D. et al. Sequential generation of linear cluster states from a single photon emitter. *Nat. Commun.* **11**, 5501 (2020).
11. Sara, B. et al. Switch networks for photonic fusion-based quantum computing. Preprint at arXiv https://arxiv.org/abs/2109.13760 (2021).
12. Lindner, N. H. & Rudolph, T. Proposal for pulsed on-demand sources of photonic cluster state strings. *Phys. Rev. Lett.* **103**, 113602 (2009).
13. Gheri, K., Saavedra, C., Törmä, P., Cirac, J. & Zoller, P. Entanglement engineering of one-photon wave packets using a single-atom source. *Phys. Rev. A* **58**, R2627 (1998).
14. Thomas, P., Ruscio, L., Morin, O. & Rempe, G. Efficient generation of entangled multiphoton graph states from a single atom. *Nature* **608**, 677–681 (2022).
15. Appel, M. H. et al. Entangling a hole spin with a time-bin photon: a waveguide approach for quantum dot sources of multiphoton entanglement. *Phys. Rev. Lett.* **128**, 233602 (2022).
16. Cogan, D., Su, Z.-E., Kenneth, O. & Gershoni, D. Deterministic generation of indistinguishable photons in a cluster state. *Nat. Photon.* **17**, 324–329 (2023).
17. Coste, N. et al. High-rate entanglement between a semiconductor spin and indistinguishable photons. *Nat. Photon.* **17**, 528–587 (2023).
18. Schwartz, I. et al. Deterministic generation of a cluster state of entangled photons. *Science* **354**, 434–437 (2016).
19. Tiranov, A. et al. Collective super- and subradiant dynamics between distant optical quantum emitters. *Science* **379**, 389–393 (2023).
20. Chen, Y., Zopf, M., Keil, R., Ding, F. & Schmidt, O. G. Highly-efficient extraction of entangled photons from quantum dots using a broadband optical antenna. *Nat. Commun.* **9**, 2994 (2018).
21. Lee, J. P. et al. A quantum dot as a source of time-bin entangled multi-photon states. *Quantum Sci. Technol.* **4**, 025011 (2019).
22. Tiurev, K. et al. Fidelity of time-bin-entangled multiphoton states from a quantum emitter. *Phys. Rev. A* **104**, 052604 (2021).
23. Bodey, J. H. et al. Optical spin locking of a solid-state qubit. *npj Quantum Inf.* **5**, 95 (2019).
24. Bechtold, A. et al. Three-stage decoherence dynamics of an electron spin qubit in an optically active quantum dot. *Nat. Phys.* **11**, 1005–1008 (2015).
25. Gangloff, D. A. et al. Quantum interface of an electron and a nuclear ensemble. *Science* **364**, 62–66 (2019).
26. Arcari, M. et al. Near-unity coupling efficiency of a quantum emitter to a photonic crystal waveguide. *Phys. Rev. Lett.* **113**, 093603 (2014).
27. Tiecke, T. G. et al. Efficient fiber-optical interface for nanophotonic devices. *Optica* **2**, 70–75 (2015).
28. Wang, Y. et al. Deterministic photon source interfaced with a programmable silicon-nitride integrated circuit. *npj Quantum Inf.* **9**, 94 (2023).
29. Appel, M. H. et al. Coherent spin-photon interface with waveguide-induced cycling transitions. *Phys. Rev. Lett.* **126**, 013602 (2021).
30. Tiurev, K. et al. High-fidelity multiphoton-entangled cluster state with solid-state quantum emitters in photonic nanostructures. *Phys. Rev. A* **105**, L030601 (2022).
31. Appel, M. H. *A Quantum Dot Source of Time-Bin Multi-Photon Entanglement*. Ph.D. thesis, https://nbi.ku.dk/english/theses/phd-theses/martin-hayhurst-appel/Martin_Hayhurst_Appel.pdf. (University of Copenhagen, 2021).
32. Stockill, R. et al. Quantum dot spin coherence governed by a strained nuclear environment. *Nat. Commun.* **7**, 12745 (2016).
33. Gühne, O., Lu, C.-Y., Gao, W.-B. & Pan, J.-W. Toolbox for entanglement detection and fidelity estimation. *Phys. Rev. A* **76**, 030305 (2007).
34. Uppu, R. et al. Scalable integrated single-photon source. *Sci. Adv.* **6**, eabc8268 (2020).
35. Chan, M. L. et al. On-chip spin-photon entanglement based on photon-scattering of a quantum dot. *npj Quantum Inf.* **9**, 49 (2023).
36. Gühne, O. & Seevinck, M. Separability criteria for genuine multiparticle entanglement. *N. J. Phys.* **12**, 053002 (2010).
37. Zaporski, L. et al. Ideal refocusing of an optically active spin qubit under strong hyperfine interactions. *Nat. Nanotechnol.* **18**, 257–263 (2023).
38. Ollivier, H. et al. Hong-Ou-Mandel Interference with Imperfect Single Photon Sources. *Phys. Rev. Lett.* **126**, 063602 (2021).

39. Wang, H. et al. Towards optimal single-photon sources from polarized microcavities. *Nat. Photonics* **13**, 770–775 (2019).
40. Somaschi, N. et al. Near-optimal single-photon sources in the solid state. *Nat. Photonics* **10**, 340–345 (2016).
41. González-Ruiz, E. M. *Single-photon sources as a key resource for developing a global quantum network.* Ph.D. thesis, https://nbi.ku.dk/english/theses/phd-theses/eva-maria-gonzalez-ruiz/eva-maria-gonzales-ruiz.pdf. (University of Copenhagen, 2023).
42. Borregaard, J. et al. One-way quantum repeater based on near-deterministic photon-emitter interfaces. *Phys. Rev. X* **10**, 021071 (2020).
43. Hummel, T. et al. Efficient demultiplexed single-photon source with a quantum dot coupled to a nanophotonic waveguide. *Appl. Phys. Lett.* **115**, 021102 (2019).

Author contributions
The experiments were conceived by P.L. and A.S. and carried out by Y.M., M.L.C., R.N., and M.A. The data analysis was performed by Y.M., M.L.C., and R.N. with support from A.S. and P.L. The experimental simulation was carried out by Y.M., M.L.C., and R.N. The quantum dot device was fabricated by N.B., A.L., and A.W. The photonic structure was designed and fabricated by A.T., Z.L., Y.W., and L.M. The paper was written by Y.M., M.L.C., P.L., and A.S.

Competing interests
P.L. is a founder of the company Sparrow Quantum which commercializes single-photon sources. The authors declare no other conflicts of interest.

Additional information
Supplementary information The online version contains supplementary material available at https://doi.org/10.1038/s41467-024-52086-y.

Correspondence and requests for materials should be addressed to Peter Lodahl.

Peer review information *Nature Communications* thanks the anonymous reviewer(s) for their contribution to the peer review of this work. A peer review file is available.

Reprints and permissions information is available at http://www.nature.com/reprints

Publisher's note Springer Nature remains neutral with regard to jurisdictional claims in published maps and institutional affiliations.